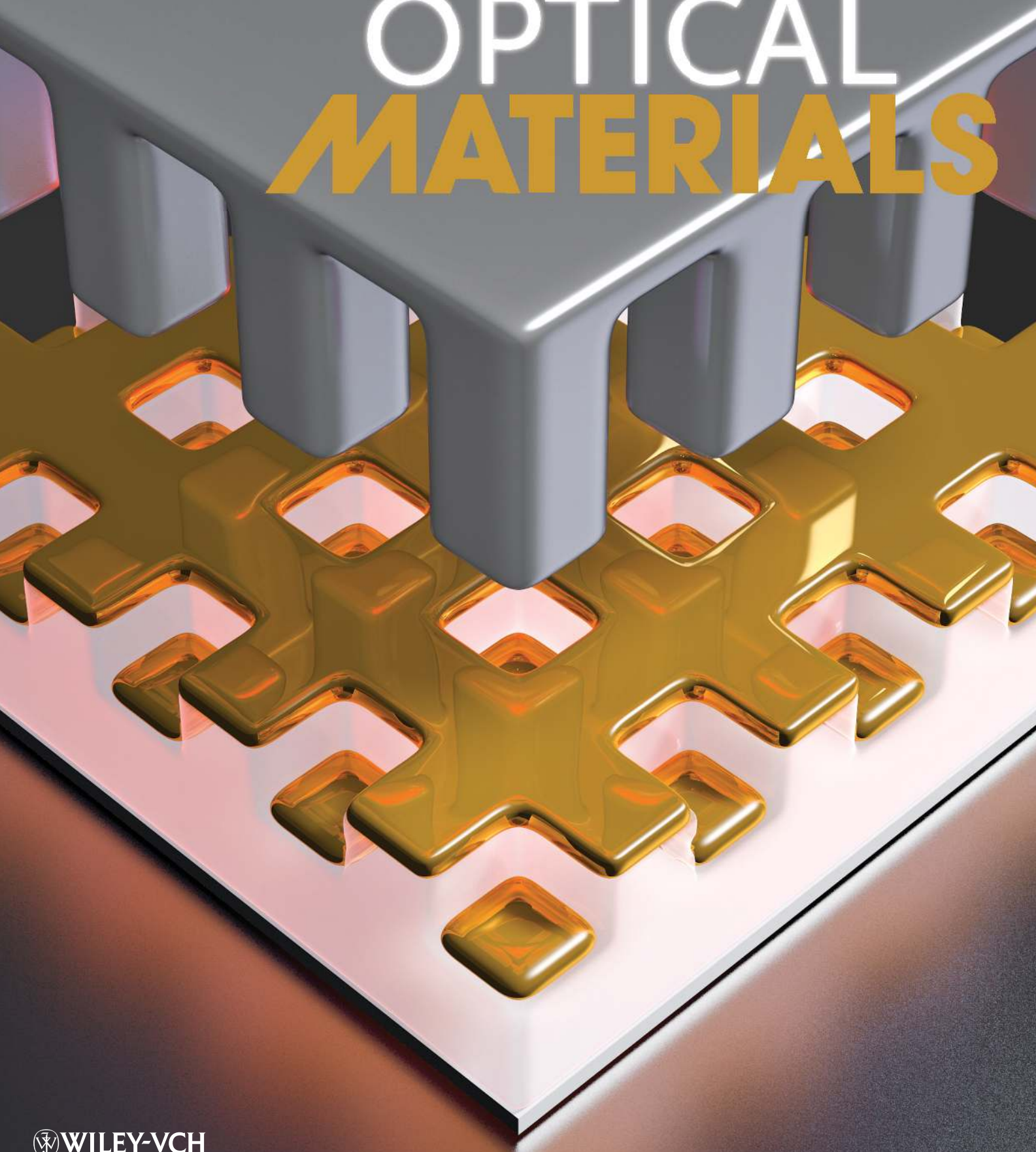# ADVANCED
OPTICAL
MATERIALS

Large-Area Gold/Parylene Plasmonic Nanostructures Fabricated by Direct Nanocutting

Vaida Auzelyte,* Benjamin Gallinet, Valentin Flauraud, Christian Santschi, Shourya Dutta-Gupta, Olivier J. F. Martin, and Juergen Brugger*

During the past decade, nanostructuring of metal surfaces has become the cornerstone of many growing fields of nanoscience and technology, such as nanoelectronics,[1] nano-electromechanical systems (NEMS),[2] plasmonics, and metamaterials.[3–5] To carry new technologies forward to their breakthrough, new patterning techniques are required to fulfil their meticulous fabrication requirements in terms of resolution, complexity, cost efficiency, and throughput. This difficulty is most prominent when aiming for mass-fabricated devices that need large surface areas covered with nanopatterns. In this regard, significant progress has recently been achieved using technologies based on various alternative patterning approaches such as soft lithography, nanosphere lithography, shadow-mask stencilling, as well as interference and nanoimprint lithographies.[6–9]

Methods, such as focused ion beam (FIB) milling[10] and electron-beam lithography (EBL)[11] have been successfully applied for extremely precise fabrication. However, those techniques suffer from their serial nature, resulting in high costs and poor throughput. For plasmonic and metamaterial applications, in particular for photovoltaic[12] and sensing devices,[13] a precise and cost-efficient fabrication of nanostructures on large areas is essential in order to emerge from the experimental stage into real-life applications. In contrast, replication-based techniques enable surface patterning over large areas. Due to its high resolution and versatility, nanoimprint lithography (NIL) is one of the most promising technologies.[14,15] Applying NIL in combination with additional post-processes such as lift-off, reactive ion etching, or various deposition techniques, gold[16,17] and silver[18] plasmonic structures, as well as Ag/SiO$_x$/Ag[19] and PZT/Au/PZT[20] multilayered nanostructures, have already been realized.

NIL can also be used for the patterning of metal surfaces without additional post-processing steps, making the fabrication process much simpler. Metals can be imprinted directly at

room[21] or at high temperatures, which is typically achieved by using resistive[22] or laser heating[23] in order soften the metal. Direct metal patterning using NIL without a resist layer is performed by applying a high pressure between the stamp and the substrate until the pattern transfer is completed. At temperatures up to about 400 °C, this method is unfortunately limited to soft metals. At higher temperatures harder metal can be patterned, but both cases result only in corrugated surface textures, which restricts its versatility.

Microcutting, a further imprint-based replication technique, has been used to pattern stratified substrates. Only moderate pressure and temperature are needed in order to obtain patterns down to the sub-micrometer range using a single imprinting step.[24] After deposition of a thin metal film overlaying a polymer, a silicon master containing edged patterns is used to cut the structures in the metal. During that transfer process, a temperature above the glass-transition temperature T$_g$ of the polymer is required for optimal results. Using this technique, micro and sub-micrometer scale structures have been replicated into gold-palladium and aluminium films.[25,26]

In this work we demonstrate metal multilayer patterning and improve the resolution of the cutting technique to the sub-100 nm range, which enables the fabrication of plasmonic structures in the visible range over large area. For demonstration purposes a thin gold layer deposited on parylene C is nanostructured using the new nanocutting technique presented in this work. Moreover, optical characterization of the realized structures together with numerical simulations show the excitation spectra of highly tunable plasmonic resonances in the visible range. In contrast to conventional nanoimprint lithography with subsequent metallization and lift-off, nanocutting allows electrical isolation of patterns located at the different indentation depths and, hence, enables the fabrication of more sophisticated structures supporting plasmonic Fano-type resonances within minutes.[27,28]

A bilayer consisting of 2 μm-thick parylene C (poly(chloro-*p*-xylylene C)) and overlaying 40 nm-thick Au film was deposited on a glass substrate by chemical vapor deposition (CVD) and electron-beam evaporation, respectively. Parylene C is a thermoplastic, semicrystalline, biocompatible, chemically inert and, most importantly, optically transparent polymer. This allows post-processing of the nanocut structures and, furthermore, their integration into optical or electrical systems on rigid and flexible substrates. Parylene C is routinely used in electronic devices as anticorrosive and dielectric layer, for instance, in organic field-effect transistors (OFET).[29] Parylene C has been tested for replication of microstructures.[30] However, to the best of our knowledge, it has neither been exploited

Dr. V. Auzelyte, V. Flauraud, Prof. J. Brugger
Microsystems Laboratory
École Polytechnique Fédérale de Lausanne (EPFL)
1015, Lausanne, Switzerland
Dr. B. Gallinet, Dr. C. Santschi, S. Dutta-Gupta,
Prof. O. J. F. Martin
Nanophotonics and Metrology Laboratory
École Polytechnique Fédérale de Lausanne (EPFL)
1015, Lausanne, Switzerland
E-mail: vaida.auzelyte@epfl.ch

for nanoscale patterning, nor for nanoimprint. During the patterning step the underlying polymer is kept above T_g because the polymer becomes a viscous liquid at that temperature. The T_g of parylene C lies between 90 and 110 °C and is, thus, similar to that of poly(methyl methacrylate) (PMMA); however, its melting temperature (T_m = 290 °C) is higher than that of PMMA (T_m = 160 °C). In addition, parylene C has a Young's modulus of E = 0.35 GPa[31] at room temperature, which is lower than that of other nanoimprinting materials, therefore allowing an imprint at lower temperatures. Lower imprint temperature is highly beneficial for imprint of metal/polymer bilayers since the risk of metal–film delamination is strongly reduced due to the lowering of the shear stress at the metal/polymer interface.[24] Furthermore, imprinting at elevated temperatures rather leads to plastic deformation of the metal–film than a to a clean cut, since the yield strength is diminished under such conditions.[32] The mentioned properties define a temperature window limited by the hardness of the polymer at low temperature and the metal film delamination at high temperature. A proper metal nanocutting is achieved at temperatures where the viscosity of the polymer is low enough for an abrupt vertical metal displacement. This is in contrast to elastic deformation that would take place at elevated working temperatures causing a viscous liquid-like state in the underlying polymer. Finally, the thickness of the polymer layer should be significantly higher with respect to that of the Au layer and the protrusion height of the stamp in order to minimise deformation of the overlaying metal layer due to lateral polymer displacement and front flow.

In order to study local plasmon resonance, a three-dimensional dot metal pattern was realized. The silicon stamps with the periodic checkerboard patterns of the corresponding sizes with 170 and 220 nm protrusion heights were fabricated using EBL with a subsequent chlorine-chemistry dry-etching (RIE) step. Periodic Au nanostructures of various sizes ranging from 55 to 500 nm were successfully patterned by direct nanocutting of a 40 nm Au film deposited on a 2 μm thick parylene C layer. A succession of nanocuts was made to optimize the imprinting temperature resulting in an ideal temperature ranging from 120 to 140 °C. A schematic drawing of the imprinting process is shown in **Figure 1**a–d. The stamp/sample assembly is kept under pressure while the temperature is increased from ambient temperature to 120–140 °C, corresponding to a temperature of
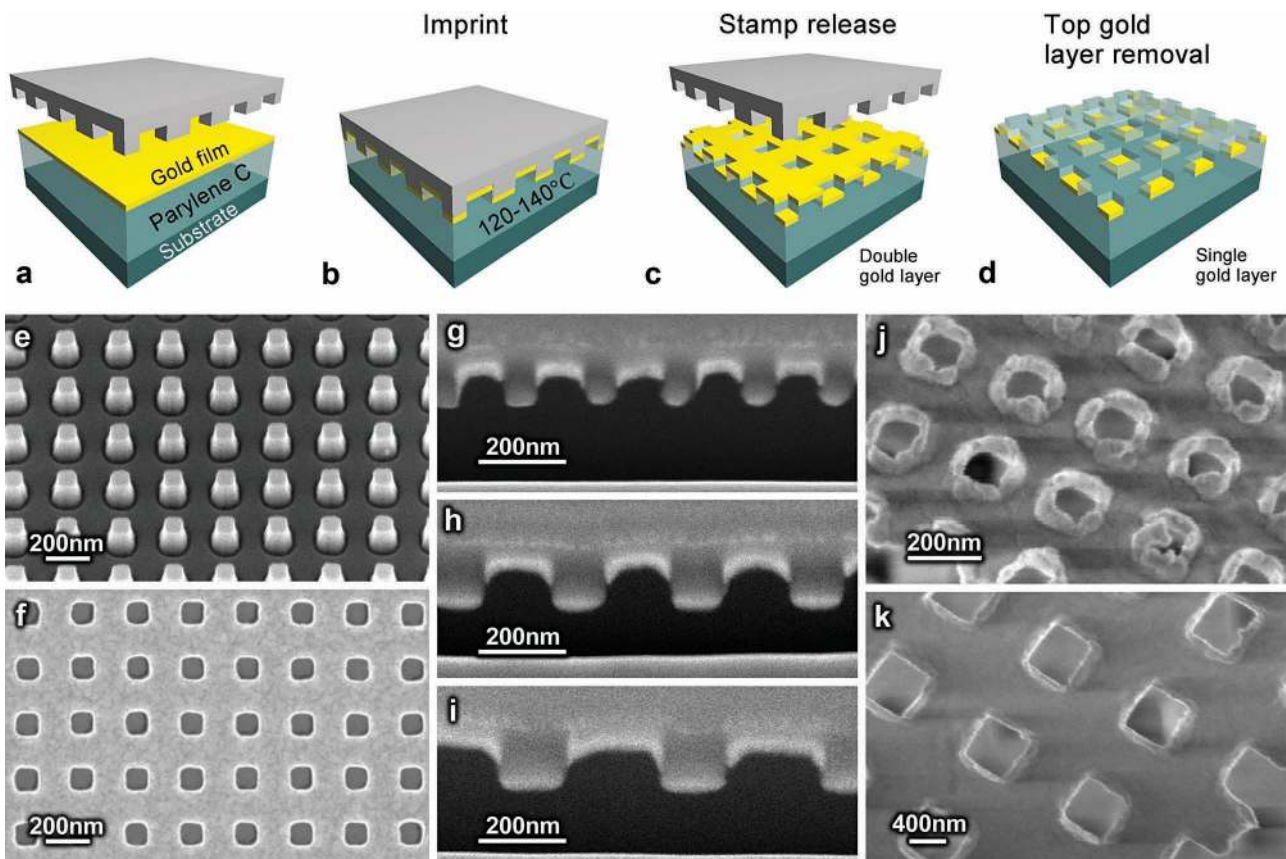

Figure 1. a-d) Schematic drawing of the metal nanocutting process: a) a Au film is deposited on a parylene C layer; b) imprinting at 120–140 °C using a silicon stamp; c) double metal layer patterns are realized after stamp release; d) removal of the top metal layer (grid) leaving a single-layer metal pattern embedded in the parylene C film; e) 250 nm period silicon stamp and f) corresponding pattern nanocut into 40 nm of Au deposited on a 2 μm thick parylene C film. The brighter and darker parts correspond to the top grid layer and the Au dots embedded in the parylene C, respectively. g-i) FIB cross-sections of the 200, 300, and 500 nm period double metal layer patterns showing the profiles and well-defined separations between the top and bottom metal layers. The separation is 40 ± 5 nm; j,k) SEM images of 250 and 600 nm period Au grids taken from the reverse side after nanocutting and delamination, showing the metal ruptures at the edge of the pattern.

COMMUNICATION

30–50 °C above the T_g of parylene C. At this temperature, the overlaying metal is deformed, breaks under pressure, and is finally pushed into the polymer to a depth that depends on the protrusion height of the stamp. The scanning electron micrographs of a typically used silicon stamp and corresponding nanocut into Au film are shown in Figure 1 e,f. Moreover, the size and shape of the patterns are well replicated in this process (see Supporting Information).

Using different protrusion heights, the vertical separation between the original and indented layers can be accurately controlled. Two electrically separated layers of Au structures are realized in this way, namely, a pattern at the top with its corresponding negative pattern underneath. Figure 1g–i shows SEM images of FIB cross-sections of 200, 300, and 500 nm periodic checkerboard patterns printed into Au/parylene C bilayers. The top and embedded Au layers are well separated and electrically isolated (different layer charging under an electron beam). Due to polymer displacement during the imprinting, the edges of the Au pattern are deformed following the movement of the stamp prior to the rupture. The typical polymer flow behavior can clearly be seen in Figure 1g and h, where a single-peak polymer front flow under the Au formed a slightly convex shape. Larger patterns of 500 nm period (Figure 1i) form relatively horizontal top Au layers. Using a stamp with protrusions of 170 nm, gaps of 40 ± 5 nm (measured between the tip of the top Au layer and the flat bottom Au layer) were achieved indicating nicely the occurrence of plastic deformation prior to the cut.

Sharp edges and vertical walls of a stamp are beneficial for a good pattern quality, but the texture of the Au film also plays an important role in terms of resolution and reproducibility. Figures 1j and k show close-up views of a checkerboard Au pattern with periods of 250 and 600 nm after removal from the underlying substrate. The rough edges of the 250 nm period pattern present a critical nanocut size. A Au film average grain size of 60 nm was determined using atomic fore microscopy (AFM) (see Supporting Information). The roughness of the rupture line and the minimal feature size achieved by nanocutting is comparable with the average grain size of the Au film, suggesting that the fracture takes place at the grain boundaries, which is consistent with known polymer-supported metal–film fracture mechanisms.[33] Therefore, the grain size of the Au film can be considered as a limiting factor for the resolution.

Single-layer structures were realized by removing the top metal layer with adhesive tape after nanocutting (Figure 1d). The examples of periodic patterns of 55 nm and 500 nm size squares with 200 nm to 1 μm periods using nanocutting are shown in **Figure 2**. Tilted micrographs of both double and single-layer checkerboard patterns with 1 μm periods and top down of 200 nm periods are shown in Figure 2 a,b and c,d, respectively. The tilted images show a clear separation between the top Au layer and into parylene C embedded bottom Au layer.

The optical response of the single-layer gold nanostructures was measured in extinction using an inverted microscope in the bright field configuration. The extinction spectra corresponding to the typical 55–115 nm sized and 200–400 nm periodic square-pattern structures are shown in **Figure 3**. The plasmon resonance of the individual dots in the single-layer configuration induces a strong light scattering and is at the origin of the
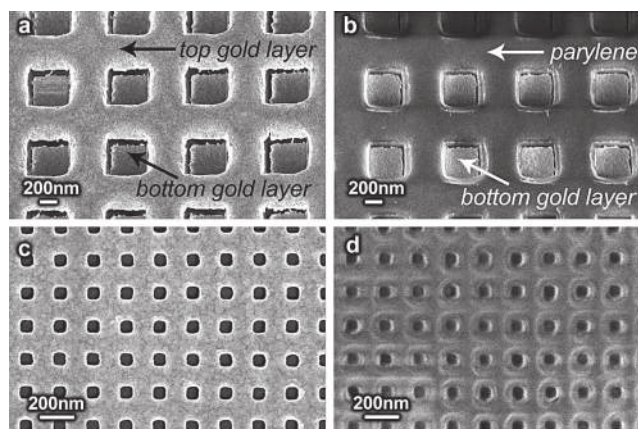

Figure 2. 30° tilted SEM images of a 1 μm periodic Au pattern fabricated using nanocutting before (a) and after (b) removal of the top Au layer, respectively, showing the separation between the top and bottom Au layers; c,d) 55 nm size and 200 nm periodic double-layer (c) and single-layer (d) Au nanostructures nanocut into and embedded in parylene C film. The nanocutting was made with a 220 nm high silicon stamp.

extinction peak. Due to their square symmetry, the individual dots support two plasmon modes resonating at the same frequency, each one corresponding to a polarization of the incident light. The dots' optical properties are therefore polarization independent. The near-field distribution displayed in the inset of Figure 3a shows that the electric field intensity in a single-layer dot array is localized at the dots' extremities, partially in the parylene C substrate, corresponding to a dipolar distribution of free charges in the metal. The optical properties of plasmon resonances are highly sensitive to the shape and dimensions of the metallic nanoparticles. As the dot size is increased from 60 nm to 115 nm, its resonance red shifts from $\lambda = 650$ nm to 815 nm (Figure 3b). In Figure 3a, an experimental extinction spectrum of the dots array without the top layer is compared to surface integral numerical simulations. The very good agreement between the positions of the extinction peak confirms that the metallic dots are well separated from the top layer and hence the geometrical properties of the bottom layer are not affected by its removal. In order to perform measurements at normal incidence, light was collected over a 20 μm × 20 μm area of structures in the array. A variation of the dimensions of the individual dots in the array reaching ±7 nm induces, with respect to simulations, an inhomogeneous broadening of the extinction peak (see Supporting Information). Additional broadening may arise from Au film and dot edge roughness.

The extinction spectrum of an infinite metallic film is close to unity for wavelengths above 700 nm, going along with the perfect reflection of gold. However, the patterned double-Au-layer system shows an extinction dip at $\lambda = 750$ nm for a 55 nm dot size and at $\lambda = 820$ nm for a 100 nm dot size. Figure 3c shows the extinction spectra of double layer structures imprinted with a 220 nm deep stamp. Under the applied nanocutting conditions, the top layer is bent as mentioned above and results in a three-dimensional geometry. This configuration not only supports dipolar plasmon modes like in the case of individual dots (Figure 3a and b), but also modes with quadrupolar charge distributions (Figure 3c). The excitation of the subradiant
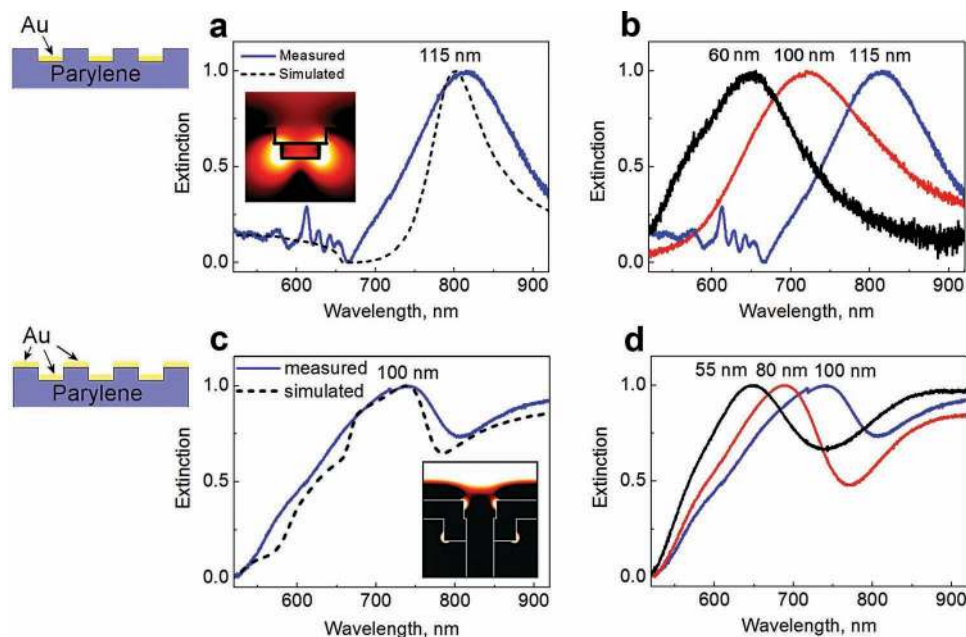
Materials
Views
www.MaterialsViews.com

ADVANCED
OPTICAL
MATERIALS
www.advopticalmat.de

Figure 3. Extinction spectra of nanocut patterns with various sizes and periods acquired at normal incidence: a,b) single-dot layers and c,d) double layers consisting of dots and a grid of Au nanostructures on parylene C film; a) measured and simulated extinction spectra of single 115 nm size and 400 nm period dot layer. Inset: electric field intensity enhancement at a wavelength of 815 nm in the vicinity of a single dot; the plane of the sampling contains the dot's centre; logarithmic scale, (black) low intensity, (white) high intensity. b) Measured extinction of the single layer with dot sizes and periods of 60, 100, and 115 nm and 200, 300, and 400 nm, respectively. c) Measured and simulated extinction spectra of 100 nm sized and 250 nm period double layers. Inset: electric field intensity enhancement in the vicinity of a single hole at a wavelength of 750 nm; the plane of sampling contains the hole's centre; logarithmic scale, (black) low intensity, (white) high intensity. d) Extinction spectra of double layer nanostructures with a separation distance between the top and bottom layer of 120 nm.

quadrupolar mode leads to the opening of a transmission window (Figure 3d). The resulting extinction spectra exhibit a Fano-like line shape[27,28] and, keeping the period constant, the resonance frequency of the transmission window can be tuned by the hole size, in a similar way as for the plasmons of the dots shown in Figure 3b. In Figure 3c, an experimental extinction spectrum is compared with numerical simulations: the position of the extinction dip at 770 nm is well reproduced. Variations of the dimensions in the fabricated array result in an inhomogeneous broadening of its line shape.[28] The inset of Figure 3c shows that a larger proportion of the electric field is localized in the air region and is, therefore, effectively accessible to molecules in, for example, biosensing or surface-enhanced Raman scattering (SERS) applications.[27]

In summary, a high-resolution and simple Au nanocutting method using a single-step nanoimprint technique is presented. Periodic Au nanopatterns in single- and double-layer configurations down to sub-100 nm sizes supporting plasmon resonances in the visible range were fabricated. It has been shown that these plasmon resonances can be tuned in the visible spectrum from green to the red. The excellent agreement between numerical simulations and optical extinction measurements evidences a very good control of the nanostructure geometry and dimension. The presented method is up-scalable and especially well adapted for large area patterning of metals, composites and alloys in single and multilayer configurations. Furthermore, it is highly versatile in terms of pattern shape and

size. It can be extended to other metals such as aluminium or silver to cover the higher frequency range of the visible spectrum. This method allows a precise control of the vertical separation between base and indented metal layers, enabling the fabrication of multilayered optically coupled structures with tailored optical response towards large scale fabrication of three-dimensional metamaterials.

Experimental Section

Stamp Fabrication: Electron beam lithography (EBL) and reactive ion etching (RIE) was used to realize the nanoimprinting stamps. 100 nm thick HSQ (Dow Corning) negative resist was structured using a 100 keV electron beam and subsequently developed. The pattern was transferred into the silicon substrate using anisotropic Cl_2-plasma etching. Prior to the imprint step the stamps were silanized using trichloro(*1H,1H*,2H,2H-perfluorooctyl)silane in the vapor phase.

Sample preparation: Glass substrates were dehydrated, activated in oxygen plasma and silanized in an IPA solution of gamma-methacryloxypropyltrimethoxysilane (A174). 2 μm of parylene C was deposited by CVD at room temperature in a vacuum chamber followed by electron-beam deposition of a 40 nm thick Au layer. No adhesion layer was used between parylene C and Au.

Nanoimprinting: The imprinting was carried out at 120–140 °C using an EHN-3250 (Microelectronic Engineering Co., Japan) thermal imprinter. The imprinter includes a vertical air-pressurized driving cylinder with maximum force of 4 kN and a hotplate. Both stamp and sample are first put under working pressure of 2 bar prior to launch the temperature ramp. Once the end temperature is achieved the nanoimprint lasts for

5–10 min. After completing the imprint process stamp and sample are left to cool down to 50 °C prior to the pressure release.

Optical Measurements: Transmission spectra of the samples were measured using an invered microscope (Olympus IX 71) coupled with a spectrometer (Jobin Yvon Triax 550) and normalized with respect to the spectrum of the light source. For all the measurements the structures were illuminated with unpolarised light at normal incidence. Since the data is discussed in terms of wavelength, the spectra were normalised to 0 and 1. The extinction is calculated following the relation: extinction = 1 − transmission.

Simulations: Numerical simulations were performed with a surface integral formulation-based on the method of moments.[34] A constant refractive index of 1.639 was used for Parylene C. Experimental data[35] were chosen for the refractive index of gold. Zero-order transmission was calculated in the far-field (for a distance of approximately 70 wavelengths from the array) with a discrete Fourier transform in the unit cell. Ideal geometries for the metallic dots were assumed and their dimensions estimated based on microscopy images of FIB cross sections.

AFM Measurements: Bruker's Dimension FastScan AFM in ScanAsyst mode was used to obtain the Au film surface-topography images. The Watershed image processing model was applied to determinethe average film grain size.

Supporting Information

Supporting Information is available from the Wiley Online Library or from the author.

[1] D. R. Ward, D. A. Corley, J. M. Tour, D. Natelson, *Nat. Nanotechnol.* **2011**, *6*, 33.

[2] A. Subramanian, A. R. Alt, L. Dong, B. E. Kratochvil, C. R. Bolognesi, B. J. Nelson, *ACS Nano* **2009**, *3*, 2953.

[3] W. Zhang, L. Huang, C. Santschi, O. J. F. Martin, *Nano Lett.* **2010**, *10*.

[4] D. K. Gramotnev, S. I. Bozhevolnyi, *Nat. Photonics* **2010**, *4*, 83.

[5] S. Cataldo, J. Zhao, F. Neubrech, B. Frank, C. Zhang, P. V. Braun, H. Giessen, *ACS Nano* **2011**, *6*, 979.

[6] J. P. Rolland, E. C. Hagberg, G. M. Denison, K. R. Carter, J. M. De Simone, *Angew. Chem. Int. Ed.* **2004**, *116*, 5920.

[7] M. J. K. Klein, M. Guillaumée, B. Wenger, L. A. Dunbar, J. Brugger, H. Heinzelmann, R. Pugin, *Nanotechnology* **2010**, *21*, 205301.

[8] O. Vazquez-Mena, T. Sannomiya, L. G. Villanueva, J. Voros, J. Brugger, *ACS Nano* **2010**, *5*, 844.

[9] W. Mao, I. Wathuthanthri, C.-H. Choi, *Opt. Lett.* **2011**, *36*, 3176.

[10] M. Guillaumee, L. A. Dunbar, C. Santschi, E. Grenet, R. Eckert, O. J. F. Martin, R. P. Stanley, *Appl. Phys. Lett.* **2009**, *94*, 193503.

[11] V. M. Sundaram, S. B. Wen, *J. Micromech. Microeng.* **2011**, *21*, 065021.

[12] H. A. Atwater, A. Polman, *Nat. Mater.* **2010**, *9*, 205.

[13] W. Kubo, S. Fujikawa, *Nano Lett.* **2010**, *11*, 8.

[14] S. H. Ahn, L. J. Guo, *ACS Nano* **2009**, *3*, 2304.

[15] A. Boltasseva, *J. Opt. A - Pure Appl. Opt.* **2009**, *11*, 114001.

[16] S.-W. Lee, K.-S. Lee, J. Ahn, J.-J. Lee, M.-G. Kim, Y.-B. Shin, *ACS Nano* **2011**, *5*, 897.

[17] A. Polyakov, S. Cabrini, S. Dhuey, B. Harteneck, P. J. Schuck, H. A. Padmore, *Appl. Phys. Lett.* **2011**, *98*, 203104.

[18] B. D. Lucas, J.-S. Kim, C. Chin, L. J. Guo, *Adv. Mater.* **2008**, *20*, 1129.

[19] W. Wu, E. Kim, E. Ponizovskaya, Y. Liu, Z. Yu, N. Fang, Y. R. Shen, A. M. Bratkovsky, W. Tong, C. Sun, X. Zhang, S. Y. Wang, R. S. Williams, *Appl. Phys. A - Mater. Sci. Proces.* **2007**, *87*, 143.

[20] H. L. Chen, K. C. Hsieh, C. H. Lin, S. H. Chen, *Nanotechnology* **2008**, *19*, 435304.

[21] S. W. Pang, T. Tamamura, M. Nakao, A. Ozawa, H. Masuda, *J. Vac. Sci. Technol.* **1998**, *16*, 1145.

[22] S. Buzzi, F. Robin, V. Callegari, J. F. Löffler, *Microelectron. Eng.* **2008**, *85*, 419.

[23] C. Bo, K. Chris, Y. C. Stephen, *Nanotechnology* **2010**, *21*, 045303.

[24] N. Stutzmann, T. A. Tervoort, K. Bastiaansen, P. Smith, *Nature* **2000**, *407*, 613.

[25] D. S. Liu, C. Y. Tsai, Y. T. Lu, C. K. Sung, C. L. Chung, *Microelectron. Eng.* **2010**, *87*, 2361.

[26] X. Liu, C. Luo, *J. Vac. Sci. Technol.* **2007**, *25*, 677.

[27] B. Luk'yanchuk, N. I. Zheludev, S. A. Maier, N. J. Halas, P. Nordlander, H. Giessen, C. T. Chong, *Nat. Mater.* **2010**, *9*, 707.

[28] B. Gallinet, O. J. F. Martin, *ACS Nano* **2011**, *5*, 8999.

[29] K. Diallo, M. Lemiti, J. Tardy, F. Bessueille, N. Jaffrezic-Renault, *Appl. Phys. Lett.* **2008**, *93*, 183305.

[30] Y. Sung-Won, G. Hiroshi, T. Masaharu, O. Shoji, O. Yasuhiko, M. Kinya, M. Ryutaro, *J. Micromech. Microeng.* **2007**, *17*, 1402.

[31] J. B. Fortin, T.-M. Lu, *Chemical Vapor Deposition Polymerization: The Growth and Properties of Parylene Thin Films*, Kluwer Academic Publishers, Norwell, MA, USA **2003**.

[32] S. Olliges, S. Frank, P. A. Gruber, V. Auzelyte, H. Solak, R. Spolenak, *Mater. Sci. Eng. A.* **2011**, *528*, 6203.

[33] Z. Zhang, T. Li, *Scripta Mater.* **2008**, *59*, 862.

[34] B. Gallinet, A. M. Kern, O. J. F. Martin, *J. Opt. Soc. Am. A* **2010**, *27*, 2261.

[35] P. B. Johnson, R. W. Christy, *Phys. Rev. B* **1972**, *6*, 4370.